



Cite this: DOI: 10.1039/c4ja00155a

High-precision measurement of Eu/Eu* in geological glasses via LA-ICP-MS analysis†

Ming Tang,^{*a} William F. McDonough^a and Ricardo Arevalo, Jr.^b

Elemental fractionation during laser ablation inductively coupled plasma mass spectrometry (LA-ICP-MS) analysis has been historically documented between refractory and volatile elements. In this work, however, we observed fractionation between light rare earth elements (LREEs) and heavy rare earth elements (HREEs) when using ablation strategies involving large spot sizes (>100 μm) and line scanning mode. In addition (1) ion yields decrease when using spot sizes above 100 μm; (2) (Eu/Eu*)_{raw} positively correlates with carrier gas (He) flow rate, which provides control over the particle size distribution of the aerosol reaching the ICP; (3) (Eu/Eu*)_{raw} shows a positive correlation with spot size, and (4) the changes in REE signal intensity, induced by the He flow rate change, roughly correlate with REE condensation temperatures. The REE fractionation is likely driven by the slight but significant difference in their condensation temperatures. Large particles may not be completely dissociated in the ICP and result in preferential evaporation of the less refractory LREEs and thus non-stoichiometric particle-ion conversion. This mechanism may also be responsible for Sm-Eu-Gd fractionation as Eu is less refractory than Sm and Gd. The extent of fractionation depends upon the particle size distribution of the aerosol, which in turn is influenced by the laser parameters and matrix. Ablation pits and lines defined by low aspect ratios produce a higher proportion of large particles than high aspect ratio ablation, as confirmed by measurements of particle size distribution in the laser induced aerosol. Therefore, low aspect ratio ablation introduces particles that cannot be decomposed and/or atomized by the ICP and thus results in exacerbated elemental fractionation. Accurate quantification of REE concentrations and Eu/Eu* requires reduction of large particle production during laser ablation. For the reference materials analyzed in this work, the 100 μm spot measurements of Eu/Eu* agreed with GeoRem preferred values within 3%. Our long-term analyses of Eu/Eu* in MPI-DING glass KL-2G and USGS glass BIR-1G were reproducible at 3% (2 RSD).

Received 16th May 2014
Accepted 1st July 2014

DOI: 10.1039/c4ja00155a

www.rsc.org/jaas

Introduction

Laser ablation-inductively coupled plasma-mass spectrometry (LA-ICP-MS) can provide spatially resolved, high-precision measurements of elemental concentrations. Accurate quantification by LA-ICP-MS relies on effective external and internal standard calibration to address elemental and isotopic fractionation. However, the fractionation process is matrix dependent,^{1,2} and may vary with ablation and ICP conditions.^{3–5}

Rare earth element (REE) geochemistry, such as REE normalized abundances and Eu anomalies, can provide insights into various geological processes. Europium anomalies (Eu/Eu*, defined as $\text{Eu}_N/\sqrt{\text{Sm}_N \times \text{Gd}_N}$, where the subscript *N* indicates chondrite normalized concentrations) have been

used as oxybarometers of planetary bodies^{6–8} due to the multi-valent nature of Eu under planetary redox conditions. Eu/Eu* in zircon has also been used to investigate redox potentials in magmas.⁹ A recent study¹⁰ revealed a regional correlation between Eu/Eu* and MgO in mid-ocean ridge basalts (MORBs) from the East Pacific Rise (EPR), and suggested the potential use of Eu/Eu* as an indicator of magmatic evolution and crustal recycling processes. However, accurate and high-precision *in situ* determination of REEs at low concentrations (sub-ppmw to tens of ppmw) is challenging. Complications derived from matrix effects, laser parameters and dynamics within the ablation plume and the ICP torch serve to inhibit the precision and accuracy of these measurements. Although REEs are refractory (having condensation temperatures in a gas at 10⁻⁴ atm > 1000 °C (ref. 11)), they can nonetheless be fractionated relative to one another during LA-ICP-MS analysis, leading to systematic errors even when the reference materials are compositionally well-matched with the sample unknowns. In this work, we measured REE concentrations and Eu/Eu* in glasses of various compositions (*i.e.*, SiO₂ from 45.5% to 58.6%), and characterized the

^aDepartment of Geology, University of Maryland, College Park, Maryland 20742, USA.
E-mail: tangmyes@gmail.com; Fax: +1 301 405 3597; Tel: +1 240 374 3443

^bNASA Goddard Space Flight Center, Greenbelt, Maryland 20771, USA

† Electronic supplementary information (ESI) available. See DOI: 10.1039/c4ja00155a

mechanisms and sources of REE fractionation by studying the relative impacts of different laser parameters (repetition rate, beam size and ablation pattern) and carrier gas (He) flow rates.

Laser ablation induced fractionation mechanisms

Multiple physical and chemical processes are involved in laser ablation processing. Generally, sample decomposition is induced by photon absorption, denoted as a photophysical process including both photothermal (thermal) and photochemical (non-thermal) activation.¹² Photothermal activation occurs when thermal relaxation rates are shorter than the pulse width. Photothermal activation results in thermal ablation by increasing the temperature in the radiation–matter interaction zone, leading to surface melting, sublimation and vaporization. In this case, the laser beam can be simply regarded as a heat source. On the other hand, photochemical activation results in direct bond breaking by promoting directly electrons across the bandgap on time scales shorter than phonon relaxation rates. Both thermal and non-thermal ablation mechanisms contribute to mass removal for most nanosecond- and picosecond-pulsed lasers. These two types of ablation processes may also contribute to laser induced elemental fractionation (LIEF), or non-stoichiometric ablation, *via* different mechanisms. In the case of thermal ablation, distinct thermal properties (*e.g.*, melting and boiling point) of different elements or geological matrices (*e.g.*, minerals, phases, *etc.*) give rise to preferential evaporation.^{13–15} In addition, surface melting and convection may lead to surface deformation, zone refinement of the melt, and chemical inhomogeneities of the resolidified material.^{12,16} Elemental fractionation induced by photochemical ablation may be associated with ionization potentials of elements and subsequent selective ionization during photon–electron coupling.^{12,15}

The primary drivers behind the fractionation mechanisms described above are laser parameters (*e.g.*, wavelength, intensity and pulse duration) and the physical and chemical properties of the material.¹² An example is laser ablation of brass, a notoriously challenging material to analyze by LA-ICP-MS or LA-ICP-AES. The distinct thermal and ionization properties of its two major chemical components, *i.e.*, Cu and Zn, lead to their contrasting behaviors when brass is ablated by nanosecond and picosecond lasers due to differences in condensation temperatures and electronics structures of these elements.¹⁵ Generally, the efficiency of coupling between laser energy and the sample inversely correlates with laser wavelength, pulse duration and sample transparency. High-energy photons (*e.g.*, ultraviolet and shorter wavelengths) can ionize more efficiently *via* single-photon absorption components in the sample.^{17,18} Long-pulse lasers (*e.g.*, 10^{-9} to 10^{-12} s) generate more thermal effects as a consequence of thermal relaxation within the radiation–matter interacting zone¹⁹ and plasma shielding effect.^{2,14,20,21} A laser induced plasma extending from the sample surface towards the incident radiation serves to absorb the laser energy that would otherwise couple to the sample; the absorption of incident

photons during long laser pulses causes the plume to expand and results in direct heating of the sample *via* the plasma–sample interaction. Since the work of Guillong and Günther,⁴ the particle size distribution has been recognized as another proxy of elemental fractionation because (1) elemental composition may be particle size dependent^{5,17} and (2) conversion of large particles into ions in the plasma may be incomplete and/or non-stoichiometric.^{4,22,23} Crater development has been shown to influence laser–matter interaction, particle size distribution and elemental fractionation.^{2,17,20,24} The aerosols produced can be significantly enriched in volatile elements (*e.g.*, Zn, Cd, Te, Se, Bi, *etc.*) during ablation of deep craters (depth-to-diameter ratio > 6).² Despite significant signal reduction, negligible fractionation of refractory elements (*e.g.*, REEs, Y, U, Ca, *etc.*) was observed even when the crater aspect ratios exceed 10 in Mank and Mason's study,²⁰ with fractionation between volatiles and non-volatiles dominantly attributed to plasma–sample interaction in deep craters. Moreover, González *et al.*²⁵ and Zhu *et al.*²⁶ compared scanning and spot ablation, and found that spot ablation provided better accuracy and precision, and was less matrix-dependent than scanning ablation.

Experimental

LA-ICP-MS

The measurements of REEs in multiple geological reference glasses were performed using a Thermo Finnigan Element2 (Thermo Fisher Scientific, Waltham, Massachusetts, USA), a single-collector, sector field, ICP-MS, coupled to a New Wave Research, frequency-quintupled (213 nm) Nd:YAG laser system (Electro Scientific Industries, Inc. Portland, OR, USA) in the Department of Geology, Plasma Laboratory at the University of Maryland. Detailed operating conditions are reported in Table 1.

The sampler cone and skimmer cone were cleaned to remove surface oxides each day. Both the ICP-MS and laser ablation system were allowed to warm up for 3 to 4 hours after plasma ignition. Prior to analysis, the ion lenses and ICP-MS torch position were tuned to maximize the signals on ⁴³Ca, ¹³⁹La and ¹⁸⁰Hf while maintaining $^{238}\text{U}^{16}\text{O}/^{238}\text{U} \leq 0.2\%$ during ablation of NIST612. Each analytical session was limited to no longer than 8 hours after tuning.

Each individual analysis incorporated a 30 s background acquisition followed by 90 s spot or scanning analysis. The isotopes measured include ²³Na, ²⁴Mg, ²⁷Al, ²⁹Si, ⁴³Ca, ⁴⁹Ti, ⁵⁵Mn, ⁵⁷Fe, ¹³⁹La, ¹⁴⁰Ce, ¹⁴¹Pr, ¹⁴⁶Nd, ¹⁴⁷Sm, ¹⁵³Eu, ¹⁵⁷Gd, ¹⁵⁹Tb, ¹⁶³Dy, ¹⁶⁵Ho, ¹⁶⁶Er, ¹⁶⁹Tm, ¹⁷²Yb and ¹⁷⁵Lu.

Particle size distribution measurement

The particle counter employed for this study was an Airy Technology P611, which has 6 channels of cumulative and different particle counts simultaneously, allowing for the detection of particles up to 0.3, 0.5, 0.7, 1.0, 2.0 and 5.0 microns. The counter detects about 50% of particles at 0.3 μm , but 100% at >0.45 μm . Reproducibility is better than 6%. The data are available in the ESI.†

Table 1 The instrumental operation conditions used for LA-ICP-MS analysis

New wave Nd:YAG laser parameters	
Wavelength	213 nm
Energy density	2–3 J cm ⁻²
Pulse duration	5 ns
Carrier gas	He
Ablation pattern	Single spot/line scanning
Laser beam size	55 μm, 80 μm, 100 μm, 125 μm, 150 μm, 175 μm
Repetition rate	5 Hz, 10 Hz, 20 Hz
Scanning speed	10 μm s ⁻¹
Thermo Finnigan Element2 ICP-MS parameters	
RF power	1250 W
HV	8 kV
Scan optimization	Speed
Mass resolution	300 (<i>m</i> /Δ <i>m</i>)
Detection mode	Analogue or both
Sampler cone	1.0 mm ID Al-alloy
Skimmer cone	0.7 mm ID Al-alloy
Cool gas flow	16 L min ⁻¹ Ar
Auxiliary gas flow	1.5 L min ⁻¹ Ar
^a Sample gas flow	0.8 L min ⁻¹ Ar
^a Carrier gas flow	0.6 L min ⁻¹ He
Dwell time	5 ms at masses 23, 24, 27, 29, 43, 49, 55, 57; 30 ms at masses 139, 140, 141, 146, 147, 159, 163, 165, 166, 169, 172, 175; 50 ms at masses 147, 157/158; 100 ms at masses 153

^a These gas flows were coupled at a T-junction prior to the plasma torch.

Reference materials and data reduction

The materials analyzed in this work were three basaltic USGS glasses (BHVO-2G, BIR-1G and BCR-2G) and five MPI-DING glasses including KL-2G (tholeiitic basalt), ML3B-G (tholeiitic basalt), GOR128-G (basaltic komatiite), GOR132-G (basaltic komatiite) and T1-G (andesitic quartz-diorite). The USGS reference materials BHVO-2G, BIR-1G and BCR-2G were used as external standards for calibration. The assumed values for the reference materials were taken from GeoRem (<http://georem.mpch-mainz.gwdg.de/>). Following Liu *et al.*²⁷ and Humayun *et al.*,²⁸ we applied internal standardization by assuming that the sum of major element oxides (SiO₂ + CaO + FeO + MgO + Al₂O₃ + MnO + Na₂O + TiO₂) equals 100%. The advantage of this method is that it does not require a second analytical measurement to obtain the concentration for a single element used as an internal standard. This method led to a maximum of 2% absolute overestimation of element concentrations, as K₂O and P₂O₅ were not included. All data are provided in the ESI.†

Results and discussion

Spectral matrix effects

Spectral matrix effects occur when specific isotope currents in the mass spectrum are overlapped by spectrometric species. These types of interferences include isobaric spectral overlap,

polyatomic molecular ion overlap, multiple charged species, and background contribution to the measurement of the ion current.²⁹ In addition, space charge effect, which results in beam defocusing, also contributes to the spectral matrix effect. To examine spectral matrix effects, isotopic ratios of seven REEs, which were measured prior to concentration determination, mostly agree with the true values within uncertainty (Fig. 1). These analyses were not corrected for mass fractionation, which would induce ~1% offset per amu for the REE. Although poorly resolved by the precision, the measured isotopic ratios 143/146, 147/149, 151/153 and 157/158 appear to be systematically higher than the true values. This is because when scanning 143 through 174, the magnet mass was set at 143 and 167. Within each magnet mass, the Element2 performed high voltage scan (E-scan) and reached the next mass peak by decreasing the acceleration voltage. This results in continuous sensitivity reduction when scanning from low mass to high mass, and thus elevated ratios of light isotopes to heavy isotopes.

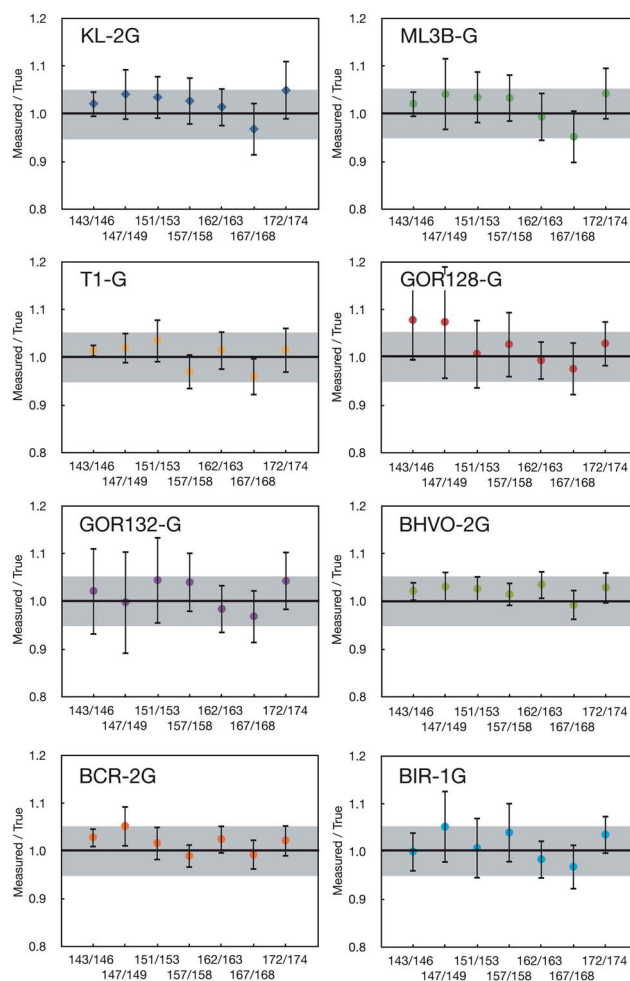


Fig. 1 Measured REE isotopic ratios compared with natural abundance ratios. The number ratios on the x-axis represent ¹⁴³Nd/¹⁴⁶Nd, ¹⁴⁷Sm/¹⁴⁹Sm, ¹⁵¹Eu/¹⁵³Eu, ¹⁵⁷Gd/¹⁵⁸Gd, ¹⁶²Dy/¹⁶³Dy, ¹⁶⁷Er/¹⁶⁸Er and ¹⁷²Yb/¹⁷⁴Yb, respectively. The error bars are 2σ_m.

Non-spectral matrix effects

Non-spectral matrix effects can be induced by non-stoichiometric sampling during laser ablation, particle loss during transport and material dissociation and ionization in the ICP. Non-spectral matrix effects may not be effectively calibrated by external standards, particularly those that are poorly matrix-matched with the sample unknowns, and result in analytical error. Understanding the mechanisms of non-spectral matrix effects and reducing their impact is key to achieving quantitative data accuracy and reproducibility. In order to reduce non-spectral matrix effects, we maintained a constant laser energy density at 2–3 J cm⁻² throughout the experiments.

Repetition rate. The repetition rate controls the rate of ablation/mass removal, and extension crater depth and crater depth-to-diameter ratio. To investigate the influence of repetition rate on LIEF, we conducted a set of 100 μm laser beam spot analyses with 5, 10 and 20 Hz repetition rate. Under these conditions, the measured REE concentrations agree with GeoRem preferred values within 10% (Fig. 2a–c). Although the signal intensities decayed 50–70% after 90 s during 20 Hz ablation, no significant REE elemental fractionation was observed.

Spot size. Ablation surface area and crater aspect ratio are associated with spot size (amongst other variables). By maintaining a constant repetition rate (10 Hz) and laser energy

density (2–3 J cm⁻²), we compared spot analyses at 55, 100 and 150 μm beam diameters (Fig. 2d and e). The 55 and 100 μm analyses yielded REE concentrations matching GeoRem preferred values within 10%. However, the HREE concentrations measured with 150 μm spots systematically deviated from the preferred values, indicating significant fractionation of HREEs from LREEs. Such elemental fractionation cannot be well calibrated even when the calibrating reference materials and sample unknowns have similar matrix compositions (*e.g.*, USGS basaltic glasses *vs.* MPI-DING basaltic glasses in this study).

Scanning mode ablation. Line scanning mode promotes low depth-to-diameter aspect ratios and stable ion beam signals (*i.e.*, minimal signal degradation *versus* time). Scanning mode ablation was examined with combinations of repetition rate (5 and 10 Hz) and beam size (55 and 100 μm) at a fixed scan rate of 10 μm s⁻¹. None of the experiments, however, gave results with acceptable overall accuracy (Fig. 3) with HREEs being significantly fractionated from LREEs, indicating non-stoichiometric sample processing.

Particle size distribution in laser induced aerosols. We measured particle size distribution in the laser-induced aerosols for BHVO-2G, NIST610 and NIST614. These reference materials cover the transparency range of most geological materials. When testing the spot mode, BHVO-2G generated low

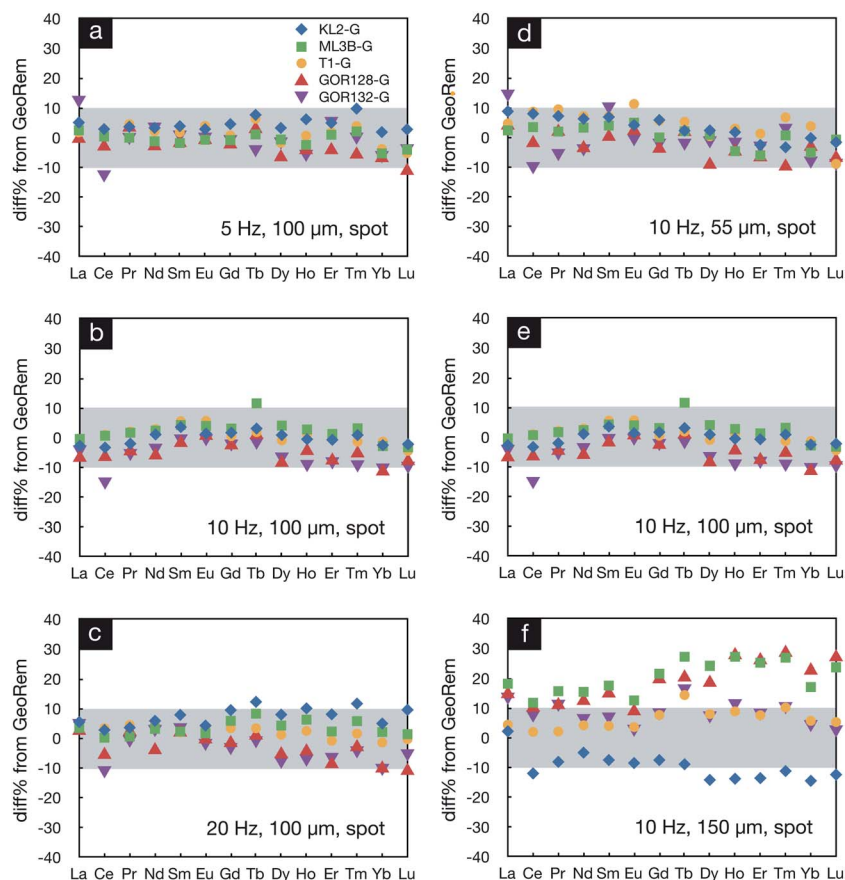


Fig. 2 Relative difference between the measured REE concentrations and GeoRem preferred values obtained in spot mode with 5, 10 and 20 Hz repetition rate at 100 μm spot size (a)–(c) and 55, 100 and 150 μm spot size at 10 Hz repetition rate (d)–(f).

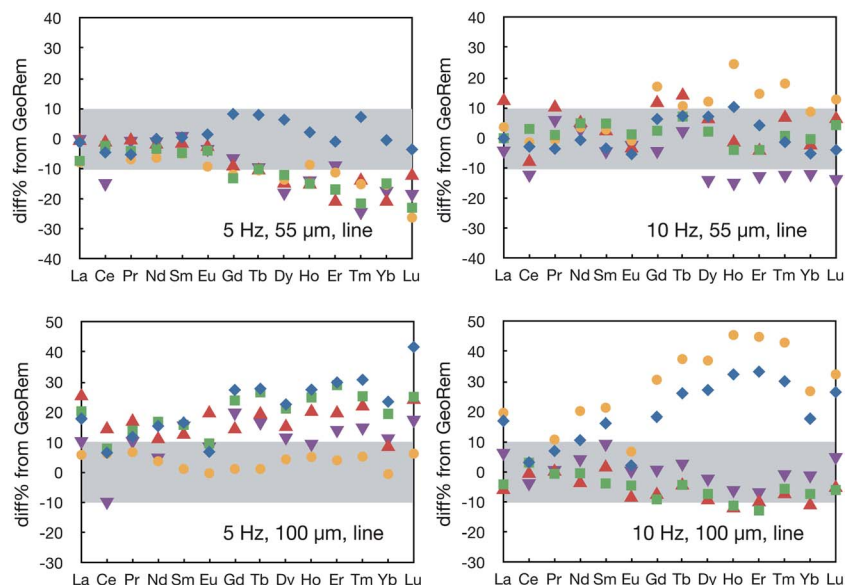


Fig. 3 Relative difference between the measured REE concentrations and GeoRem preferred values obtained in line scanning mode. Same legends as Fig. 2.

total counts for particles above 1 μm and there is no clear relationship between the proportion of large particles ($>1 \mu\text{m}$) and spot size (Fig. 4a). For NIST610, significantly greater proportions of large particles were produced, and a positive correlation between the proportion of large particles and spot size is observed (Fig. 4b). This relationship holds when using

line scanning mode on BHVO-2G with an exception at 175 μm (Fig. 5). The lack of correlation in the BHVO-2G spot mode experiment might result from counting statistics, as the majority of particles produced are likely smaller than 0.3 μm . In the experiments comparing spot mode vs. line scanning mode, we observed that, at the same beam size, significantly more large particles were produced during line scanning ablation. The particle size distribution is also dependent upon sample transparency, and more transparent samples generated a greater proportion of large particles (Fig. 6).

Assessment. The above observations lead us to conclude that (1) HREEs can be fractionated from LREEs during LA-ICP-MS analysis; (2) ablation using large laser spots ($>100 \mu\text{m}$) and line scanning mode induces significant matrix-dependent fractionation irrespective of the repetition rate and (3) low aspect ratio ablation (large spot size and line scanning) and low photon absorption (high transparency) give rise to a higher production rate for large particles.

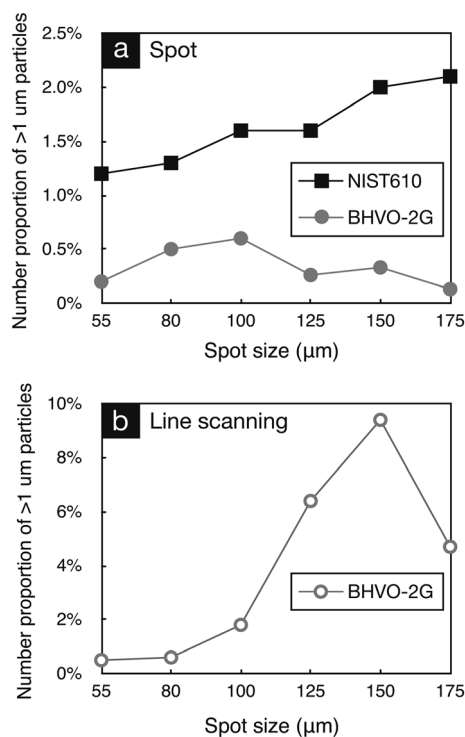


Fig. 4 Number proportion of large particles ($>1 \mu\text{m}$) vs. spot size in spot and line scanning modes.

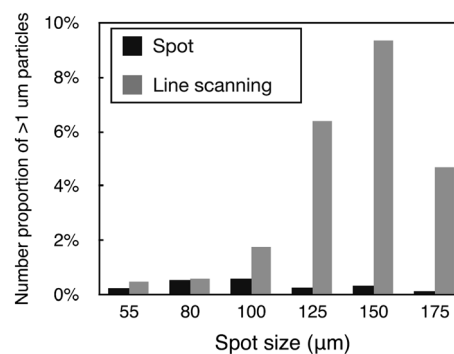


Fig. 5 Comparison of the proportion of large particles produced in spot and line scanning modes.

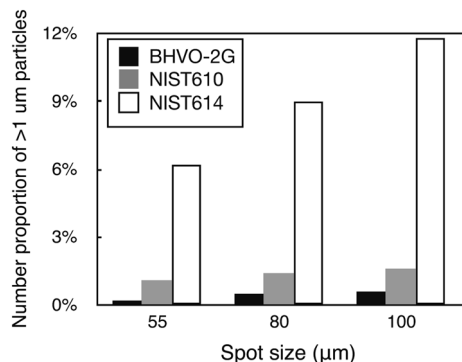


Fig. 6 Comparison of the proportion of large particles produced by samples of different transparency (photon absorption rate). Transparency increases in the order of BHVO-2G < NIST610 < NIST614. The experiments were done in spot mode.

Preferential photon–electron coupling is unlikely to account for large REE fractionation observed here due to their similar ionization potentials (*i.e.*, 5.5 to 6.8 eV). Furthermore, such fractionation was rather limited, if present, when using spot ablation with 55 and 100 μm beams (relatively large depth-to-diameter aspect ratio). The deep crater effect on REE fractionation was examined with a set of 20 Hz 55 μm spot experiments, which generated a total of 1800 shots at each spot. The measured concentrations agree with preferred values (Fig. 7). Guillong and Günther⁴ observed that even closely matched

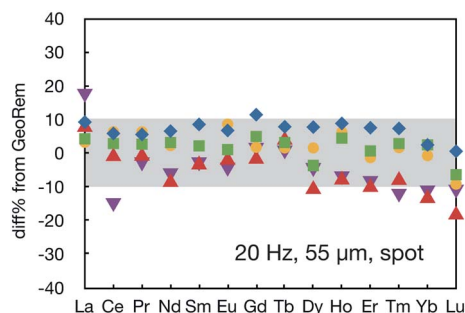


Fig. 7 Relative difference between the measured REE concentrations and GeoRem preferred values obtained in spot mode with 55 μm spot size and 20 Hz repetition rate. Same legends as Fig. 2.

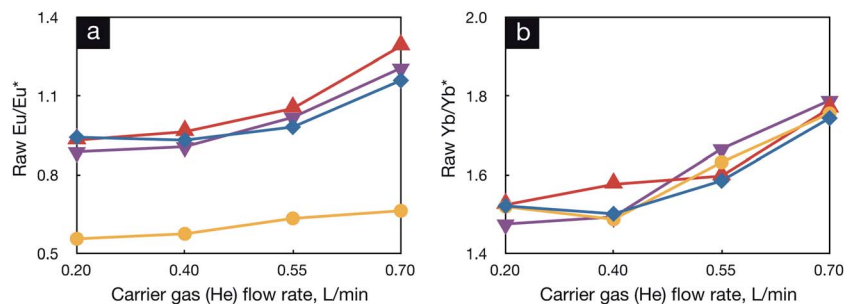


Fig. 8 Raw Eu/Eu^* and Yb/Yb^* increase with He flow rate. The $2\sigma_m$ error bars on the sensitivities are about the size of the symbols. Same legends as Fig. 2.

elements, such as Th and U, could be fractionated when a significant portion of large particles cannot be fully decomposed and excited in the ICP. The effect of particle size distribution was also emphasized by subsequent studies.^{17,25,30}

To examine the effect of particle size distribution on REE fractionation, we compared the measurements conducted under various He flow rates ($0.7\text{--}0.2\text{ L min}^{-1}$). By decreasing the He flow rate from 0.70 L min^{-1} to 0.2 L min^{-1} the signals were reduced by a factor of 2–5 (element dependent). The reduction of counts induced by lowering the He flow rate may partially result from the loss of ablated materials due to gravitational filtering of large particles during transport. Particle separation during transport inevitably leads to a change in particle size distribution. The raw Eu/Eu^* and raw Yb/Yb^* ($^{172}\text{Yb}/\sqrt{\text{cps}(^{165}\text{Tm} \cdot ^{175}\text{Lu})}$) positively correlate with He flow rate, which translates into a faster increase of Eu and Yb counts compared with their neighboring REEs. Europium and ytterbium, as well as their oxides, have lower condensation temperatures than the other REEs, and they are, irrespective of the matrix, more sensitive to He flow rate than their neighboring REEs (Fig. 8). And because He flow rate influences the particle size distribution of the aerosol reaching the ICP, the above observations point to a relationship between elemental fractionation, condensation temperature and particle size distribution. In addition to condensation temperature, electronic structures likely exert an effect on elemental fractionation,³¹ but this mechanism does not explain the correlations in Fig. 8. The link between REE fractionation and condensation temperature is further supported by the rough positive correlation between $\text{cps}_{0.2}/\text{cps}_{0.7}$ (the ratio of cps at 0.2 L min^{-1} He flow rate to cps at 0.7 L min^{-1} He flow rate) and condensation temperature (Fig. 9). The difference in condensation temperature may account for the observed LREE–HREE fractionation as LREEs are generally less refractory than HREEs.¹¹ As to melting and boiling temperatures, we found no correlation between these physical parameters and REE fractionation.

Fig. 10 plots the ion yields (cps/spot diameter squared) at various mass stations as a function of spot size (10 Hz repetition rate). The low ion yields at small spot sizes (55 and 80 μm) may result from a significant plasma shielding effect in relatively narrow craters. However, the ion yield starts to decrease when the spot size exceeds 100 μm . This negative correlation from 100 to 175 μm may reflect the reduction of ionization efficiency of

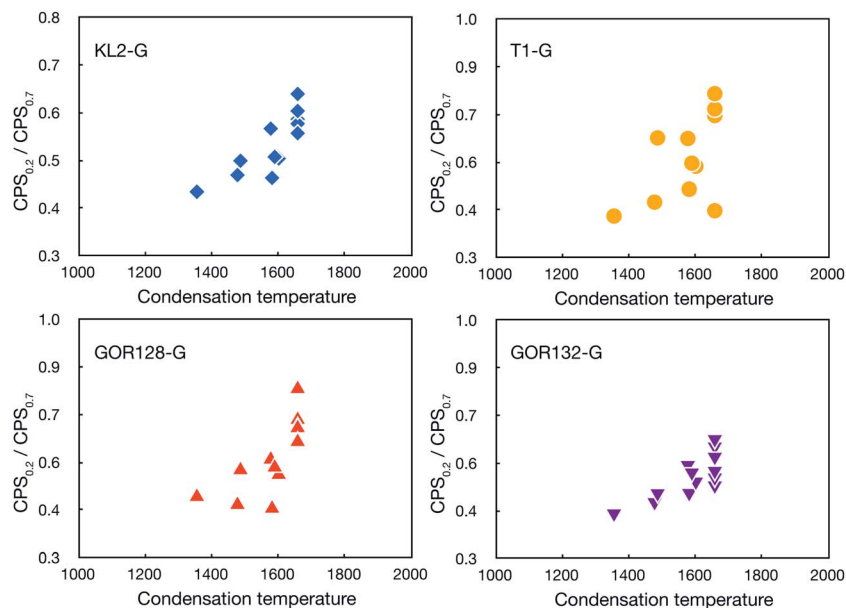


Fig. 9 Intensity change induced by He flow change vs. condensation temperature from Lodders.¹¹

aerosols in the plasma, which may be caused by the mass loading effect due to (1) the large mass flux introduced into the plasma and/or (2) the broader particle size distribution or a greater amount of large particles produced by low depth-to-diameter ablation. The formation of large particles is usually linked to surface melting and hydrodynamic sputtering,³² or

Gaussian distribution of photon density within the laser beam, the latter of which is unlikely since the laser used in this work is fluence homogenized. The measured $(\text{Eu}/\text{Eu}^*)_{\text{raw}}$ ($(\text{Eu}/\text{Eu}^*)_{\text{raw}} = {}^{153}\text{Eu}/\text{sqrt}({}^{147}\text{Sm} \cdot {}^{157}\text{Gd})$, external standard calibration not applied) in BHVO-2G increases with spot size, or the proportion of large particles (Fig. 11), suggesting that the Sm-Eu-Gd

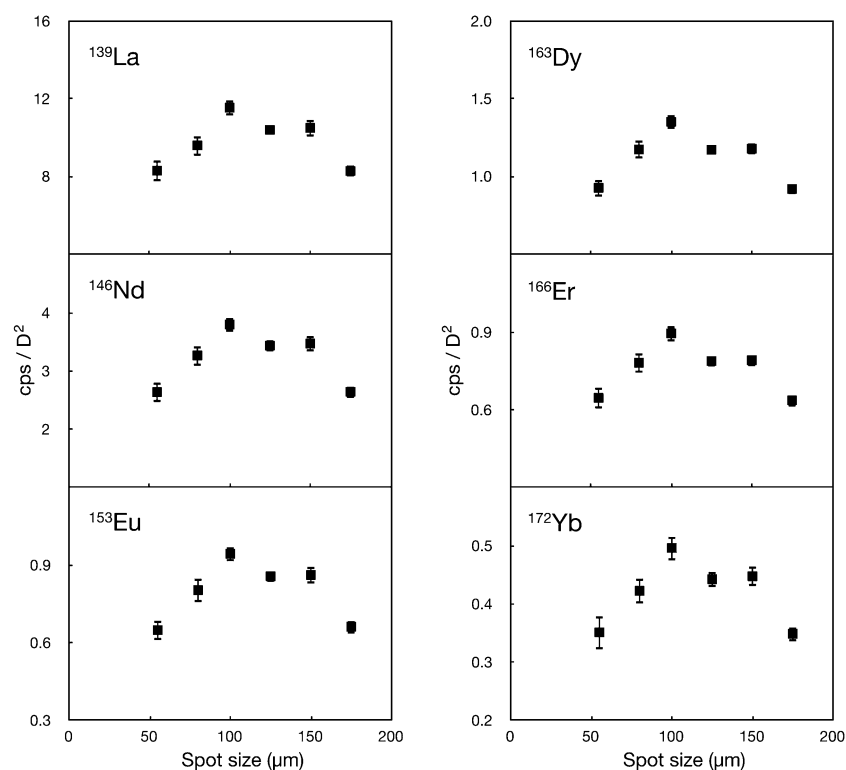


Fig. 10 Counts per second (cps) normalized to beam diameter squared (D^2), as a proxy for combined photon flux and ionization efficiency, obtained with 55 to 175 μm spots on BHVO-2G. A linear time drift calibration was applied to each analysis.

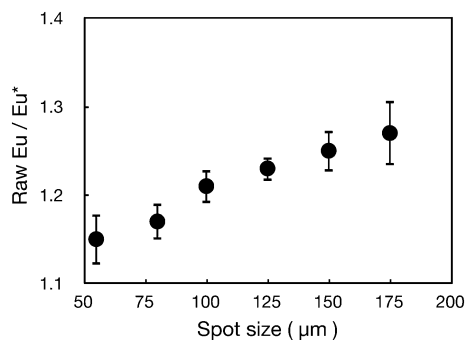


Fig. 11 Raw Eu/Eu* measured with 55 to 175 μm spots on BHVO-2G. A linear time drift calibration was applied to each analysis. The error bars are $2\sigma_m$.

fractionation is sensitive to particle size distribution. Despite more counts delivered by larger spots, the progressively more spiky signals resulted in the increasing error bars ($2\sigma_m$) from 125 to 175 μm (Fig. 11).

These observations lead us to link REE fractionation and condensation temperature. Low depth-to-diameter ratio ablation generates more large particles. The difference in condensation temperature results in non-stoichiometric ion yields if ionization of particles is non-quantitative in the ICP. It remains unclear whether or not REEs are also fractionated at the ablation site, as the chemical composition of the aerosol may also be particle size dependent. However, if this is true, given that volatile elements tend to be enriched in small particles,⁵ the intensities of the less refractory LREEs should be less sensitive to carrier gas flow rate, which is not the case (Fig. 8 and 9). Therefore, LIEF, if present, has relatively minor contribution to the fractionation observed here. To further clarify this issue, future work needs to determine REE compositions of particles collected at different size cuts.

Fig. 12 compares the measured Eu/Eu* values with GeoRem preferred values in spot (100 μm) and scanning (100 μm) mode (calibrated against BHVO-2G). The 100 μm spot measurements yielded results that agree with the preferred values within 3% while the scanning mode suffered from significant non-spectral matrix effects. The basaltic MPI-DING glasses KL-2G and ML3B-G cannot be well calibrated by the USGS standard BHVO-2G in scanning mode, which is surprising given that they are all

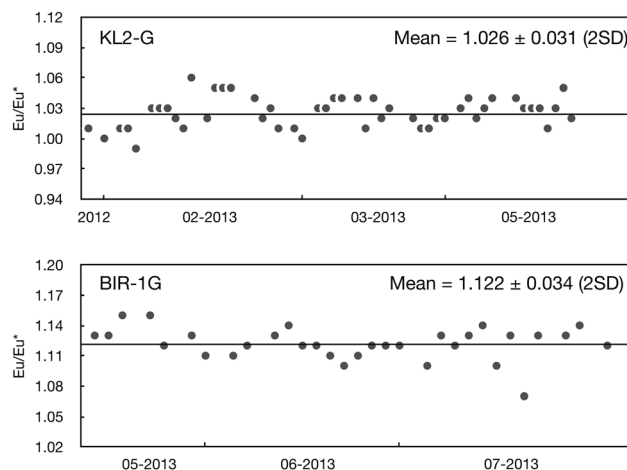


Fig. 13 Long-term analyses of Eu/Eu* in KL-2G (top panel) and BIR-1G (bottom panel). The solid lines indicate the mean values for both glasses.

Hawaiian basalts with similar bulk compositions. Particle size distribution is thus highly sensitive to even subtle difference in physical and chemical properties or the surface morphology of different matrices. Shown in Fig. 13 is our long-term measurement of Eu/Eu* in KL-2G and BIR-1G reproducible at 3% (2RSD).

Conclusions

(1) Refractory elements, such as REEs, can be fractionated during LA-ICP-MS analysis. Line scanning and spot analyses using large laser beams ($>100 \mu\text{m}$) promote statistically significant fractionation effects. Such REE fractionation is also sensitive to carrier gas flow rate and is matrix dependent;

(2) Low aspect ratio ablation (large spot size and line scanning) and low photon absorption (high sample transparency) result in production of more large particles proportionally;

(3) The primary fractionation mechanism invoked is associated with condensation temperature. Low depth-to-diameter aspect ratio ablation generates a significant amount of large particles that may be poorly decomposed and ionized in the ICP. In this case, the less refractory REEs may be preferentially evaporated and ionized. Non-quantitative ionization of particles

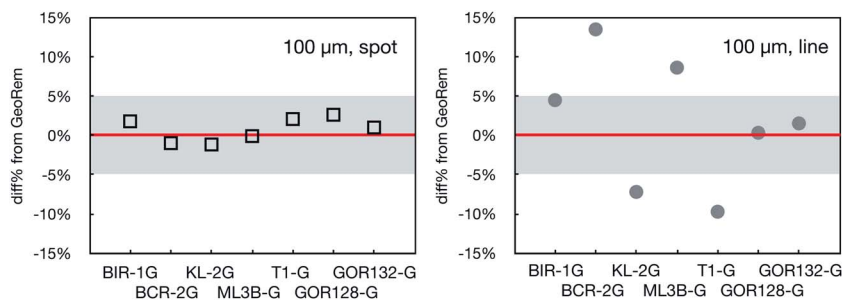


Fig. 12 Relative difference between the measured Eu/Eu* and GeoRem preferred values obtained in spot mode with 100 μm spot size and scanning mode with 100 μm spot size. The repetition rate was 10 Hz.

of various sizes may result in condensation temperature dependent REE fractionation (e.g., LREE–HREE, Sm–Eu–Gd, Tm–Yb–Lu). The extent of fractionation is sensitive to particle size distribution of the aerosol.

(4) Controlled laser parameters can minimize the production of large particles and significant REE fractionation, as demonstrated by the Eu/Eu* values in a set of reference materials which agreed with GeoRem preferred values within 3%. A long-term reproducibility of 3% (2 RSD) was achieved for Eu/Eu* in KL-2G and BIR-1G.

Acknowledgements

This work was supported by NSF grant EAR-0739006. We thank Richard Ash for assistance with LA-ICP-MS analysis. We also appreciate Yu Huang's help on data reduction.

References

- 1 J. S. Becker, C. Pickhardt and H.-J. Dietze, *Mikrochim. Acta*, 2000, **135**, 71–80.
- 2 S. M. Eggins, L. P. J. Kinsley and J. M. G. Shelley, *Appl. Surf. Sci.*, 1998, **127–129**, 278–286.
- 3 D. B. Aeschliman, S. J. Bajic, D. P. Baldwin and R. S. Houk, *J. Anal. At. Spectrom.*, 2003, **18**, 1008–1014.
- 4 M. Guillong and D. Günther, *J. Anal. At. Spectrom.*, 2002, **17**, 831–837.
- 5 H. R. Kuhn, M. Guillong and D. Günther, *Anal. Bioanal. Chem.*, 2004, **378**, 1069–1074.
- 6 G. McKay, L. Le, J. Wagstaff and G. Crozaz, *Geochim. Cosmochim. Acta*, 1994, **58**, 2911–2919.
- 7 C. Shearer, J. Papike and J. Karner, *Am. Mineral.*, 2006, **91**, 1565–1573.
- 8 M. Wadhwa, *Science*, 2001, **291**, 1527–1530.
- 9 D. Trail, E. Bruce Watson and N. D. Tailby, *Geochim. Cosmochim. Acta*, 2012, **97**, 70–87.
- 10 Y. Niu and M. J. O'Hara, *Lithos*, 2009, **112**, 1–17.
- 11 K. Lodders, *Astrophys. J.*, 2003, **591**, 1220.
- 12 D. W. Bäuerle, *Laser Processing and Chemistry*, Springer, 2011.
- 13 C. Liu, X. L. Mao, S. S. Mao, X. Zeng, R. Greif and R. E. Russo, *Anal. Chem.*, 2003, **76**, 379–383.
- 14 X. Mao, W.-T. Chan, M. Caetano, M. A. Shannon and R. E. Russo, *Appl. Surf. Sci.*, 1996, **96–98**, 126–130.
- 15 X. L. Mao, O. V. Borisov and R. E. Russo, *Spectrochim. Acta, Part B*, 1998, **53**, 731–739.
- 16 E. F. Cromwell and P. Arrowsmith, *Anal. Chem.*, 1995, **67**, 131–138.
- 17 M. Guillong, I. Horn and D. Günther, *J. Anal. At. Spectrom.*, 2003, **18**, 1224–1230.
- 18 I. Horn, M. Guillong and D. Günther, *Appl. Surf. Sci.*, 2001, **182**, 91–102.
- 19 M. C. Richardson, A. Zoubir, L. Shah, C. Rivero, C. Lopez, K. A. Richardson, N. Ho and R. Vallee, *Proc. SPIE 5273*, 2004, DOI: 10.1117/12.530684.
- 20 A. J. G. Mank and P. R. D. Mason, *J. Anal. At. Spectrom.*, 1999, **14**, 1143–1153.
- 21 M. A. Shannon, X. L. Mao, A. Fernandez, W.-T. Chan and R. E. Russo, *Anal. Chem.*, 1995, **67**, 4522–4529.
- 22 S. H. Jeong, O. V. Borisov, J. H. Yoo, X. L. Mao and R. E. Russo, *Anal. Chem.*, 1999, **71**, 5123–5130.
- 23 I. Krosiakova and D. Günther, *J. Anal. At. Spectrom.*, 2007, **22**, 51–62.
- 24 O. V. Borisov, X. Mao and R. E. Russo, *Spectrochim. Acta, Part B*, 2000, **55**, 1693–1704.
- 25 J. J. González, A. Fernández, X. Mao and R. E. Russo, *Spectrochim. Acta, Part B*, 2004, **59**, 369–374.
- 26 L. Zhu, Y. Liu, Z. Hu, Q. Hu, X. Tong, K. Zong, H. Chen and S. Gao, *Geostand. Geoanal. Res.*, 2013, **37**, 207–229.
- 27 Y. Liu, Z. Hu, S. Gao, D. Günther, J. Xu, C. Gao and H. Chen, *Chem. Geol.*, 2008, **257**, 34–43.
- 28 M. Humayun, F. A. Davis and M. M. Hirschmann, *J. Anal. At. Spectrom.*, 2010, **25**, 998–1005.
- 29 H. E. Taylor, in *Inductively Coupled Plasma-Mass Spectrometry*, ed. H. E. Taylor, Academic Press, San Diego, 2001, pp. 125–142, DOI: 10.1016/B978-012683865-7/50008-9.
- 30 A. Plotnikov, C. Vogt, K. Wetzig and A. Kyriakopoulos, *Spectrochim. Acta, Part B*, 2008, **63**, 474–483.
- 31 F. E. Jenner and H. S. C. O'Neill, *Geostand. Geoanal. Res.*, 2012, **13**, Q03003.
- 32 R. Hergenroder, *J. Anal. At. Spectrom.*, 2006, **21**, 517–524.